Fuel Processing Technology 156 (2017) 156–170

Contents lists available at ScienceDirect

Fuel Processing Technology

journal homepage: www.elsevier.com/locate/fuproc

Chemical looping reforming in packed-bed reactors: Modelling, experimental validation and large-scale reactor design

V. Spallina [a,*], B. Marinello [b], F. Gallucci [a], M.C. Romano [b], M. Van Sint Annaland [a]

[a] Chemical Process Intensification (SPI), Chemical Engineering and Chemistry Department, Eindhoven University of Technology, Eindhoven, The Netherlands
[b] Group of Energy Conversion Systems (GECOS), Department of Energy. Politecnico di Milano, Milano, Italy

ARTICLE INFO

Article history:
Received 20 June 2016
Received in revised form 8 October 2016
Accepted 9 October 2016
Available online xxxx

Keywords:
Chemical looping reforming
Packed bed reactor
Experimental validation
Modelling
Hydrogen
Methanol

ABSTRACT

This paper addresses the experimental demonstration and model validation of chemical looping reforming in dynamically operated packed-bed reactors for the production of H_2 or CH_3OH with integrated CO_2 capture. This process is a combination of auto-thermal and steam methane reforming and is carried out at high pressure, as typical for reforming processes, and at relatively low to intermediate temperatures (ranging from 600 to 900 °C). The oxidation of the oxygen carrier is performed with air and the hot depleted air stream is fed to a gas turbine, which contributes to reduce the electricity demand. After oxidation, a low-grade fuel is used for the reduction of the oxygen carrier, e.g. off-gas from a PSA unit or non-condensable species from methanol synthesis and, when the bed is completely reduced, natural gas diluted with H_2O and CO_2 is reformed while the reactor is cooled down.

An experimental campaign has been carried out in a 2 kW_{th} packed-bed reactor using 500 g of NiO supported on $CaAl_2O_4$ as reforming catalyst and oxygen carrier. This material has demonstrated very high stability over >400 h of consecutive redox and reforming cycles. Due to the flexibility of the process, dry, wet and steam reforming compositions have been tested during the reforming phase. A 1D reactor model has been validated with the obtained experimental results, including also a detailed thermal model to account for the inevitable heat losses of the system. The experimental and model results are in good agreement in terms of breakthrough curves and temperature profiles. The experimental campaign during reforming also confirmed the possibility to carry out the heat removal phase by means of endothermic methane reforming.

The validated reactor model has subsequently been used for the simulation of different configurations in terms of heat management in which the different phases (oxidation, reduction and reforming) are simulated in series. In these analyses, the reactor design and performance have been compared for two plant configurations based on H_2 and CH_3OH production integrated with CO_2 capture. For the case of H_2 production, the CH_4 conversion is 92% and all the CO_2 is captured from the plant, while for CH_3OH production the CH_4 conversion reaches 90% and all carbon species, except CH_3OH, are converted into CO_2, which is separated with high purity.

1. Introduction

Steam reforming is the established process for H_2 production [1] and for syngas production for the manufacture of methanol [2]. Natural gas reforming is carried out in multi-tubular fixed bed reactors using an external furnace to provide the heat of reaction (FTR) or in an auto-thermal reforming (ATR) system using an oxidant (i.e. air or pure oxygen) [1,3–5]. Based on the current process, the following equilibrium limited reactions of steam methane reforming (SMR (1)), and water gas shift (WGS (2)) are identified:

$$CH_4 + H_2O \rightleftarrows 3H_2 + CO \qquad \Delta H_0^{298K} = 206.2 kJ/mol \qquad (1)$$

$$CO + H_2O \rightleftarrows H_2 + CO_2 \qquad \Delta H_0^{298K} = -41.2 kJ/mol \qquad (2)$$

Conventional steam reforming processes are based on several conversion and separation steps, which include feedstock pre-treatment and removal of sulfur compounds (the catalyst used in steam reforming is extremely sensitive to sulfur and therefore the concentration is kept below 0.5 ppm), high temperature reforming, water gas shift reactor(s) and a final pressure swing adsorption (PSA) unit in order to reach a H_2 purity in the order of 99.999%. The conventional plants lead to high CO_2

* Corresponding author at: Chemical Engineering and Chemistry Department, P.O. Box 513, 5600 MB, Eindhoven, The Netherlands.
E-mail address: v.spallina@tue.nl (V. Spallina).

http://dx.doi.org/10.1016/j.fuproc.2016.10.014

emissions (about 0.8 kg_{CO2}/Nm^3H_2) to the atmosphere, because the PSA-off-gas and part of the input natural gas are burnt in the furnace to supply the heat for the endothermic reforming reaction. In order to reduce CO_2 emissions, CO_2 can be separated from the H_2-rich syngas downstream of the WGS reactor using an MDEA scrubber [6,7] or in a post-combustion capture unit at the gas stack of the reformer, where the CO_2 is separated from the exhaust gases using MEA absorption resulting in up to 90% CO_2 capture [8].

Natural gas is also the main feedstock for methanol production. Different plant layouts are considered depending on the plant size. Single-step reforming is mainly considered for plants up to 2500 MTPD (Metric Tons Per Day) capacity, while larger units (up to 10,000 MTPD) are based on a two-step reforming process, which features a combination of primary reforming (designed as an FTR) and oxygen-blown autothermal reforming using O_2 from a cryogenic air separation unit (ASU) [9]. The optimal syngas composition is reached when the so called module M (Eq. (5)) is equal to 2, which is the stoichiometric number required to reach the maximum CH_3OH yield.

$$CO + 2H_2 \rightarrow CH_3OH \qquad \Delta H_0^{298K} = -90.8 kJ/mol \tag{3}$$

$$CO_2 + 3H_2 \rightarrow CH_3OH + H_2O \qquad \Delta H_0^{298K} = -49.2 kJ/mol \tag{4}$$

$$M = \frac{(H_2 - CO_2)}{(CO + CO_2)} \tag{5}$$

After cooling to nearly ambient temperature, the reformed syngas is compressed up to 50–100 bar in a multistage compressor, heated up to above 100 °C and fed to a cooled reactor operated at about 200–300 °C. The heat of reaction is released by producing intermediate pressure steam. The CH_3OH rich stream is cooled down, condensed and the liquid is separated from the unconverted gases, which are usually recirculated back to the methanol synthesis reactor. After that, the CH_3OH is sent to different separation columns to reach the required purity of 99.9% [2]. The conventional CH_3OH production process based on ATR reaches methanol yields of 0.82 mol_{CH3OH}/mol_{CH4} with about 0.17 kg_{CO2}/kg_{CH3OH} emitted to the atmosphere from the combustion of the process off-gases [10].

Among the several emerging solutions proposed for CO_2 capture in power plants and industrial processes [11], chemical looping technology represents one of the most promising and efficient alternatives, since the CO_2 separation is inherently integrated in the primary fuel conversion step [12]. If a metal oxide (named oxygen carrier) is alternatively exposed to air (for oxidation) and to a fuel stream (for reduction), a pure CO_2/H_2O stream is produced (chemical looping combustion, CLC). If a sub-stoichiometric OC-to-fuel ratio is adopted, partial fuel oxidation is obtained and reformate syngas can be produced (chemical looping reforming, CLR). CLR has been mainly studied using Ni-based oxygen carriers, which also present catalytic activity for the steam methane reforming reactions. Based on a simplified thermodynamic analysis it has been found that H_2 yields of 2.74 $molH_2/mol_{CH4}$ are achievable when working with a NiO/CH_4 molar ratio equal to 1.18 to sustain the endothermic reactions in the fuel reactor [13].

Due to the different catalytic activity and oxygen carrying capacity, different oxygen carrier materials have been considered for the CLR process [14]. Pröll et al. [15] have presented the performances of a dual circulating fluidized bed reactor operated with Ni/NiO as oxygen carrier in a 120 kW_{th} facility operated for >90 h, reaching >90% of methane conversion. Chiron et al. [16] have performed experiments and model validation in a micro packed-bed reactor (operated with 200 mg of oxygen carrier) and they have presented a reactor configuration in which the NiO supported on Al_2O_3 is reduced in a first stage and afterward used as catalyst in a second reactor where the SMR occurs. Ortiz et al. [13,17,18] have presented both modelling and experimental demonstration of CLR in a 900 W_{th} fluidized bed unit. The experimental studies were carried out with a Ni-based catalyst and the process optimization has been undertaken by varying the steam-to-carbon ratio (S/C), the oxygen-to-carbon ratio (O/C or NiO/C), solid conversion (ΔX_s) and other relevant variables affecting the performance of the system. Different oxygen carriers have been synthetized and tested for CLR in fluidized bed configuration [19–21] and among all, the high reactivity of Ni for both fuel conversion and SMR results in the highest performances. However, the current high cost and toxicity compared with other oxygen carriers (OC) could hamper the use of Ni-based OCs. Moreover, the H_2 production process should preferably be carried out at high pressures, because industrial processes for CO_2 separation (through amine scrubbing) and purification (in a conventional pressure swing adsorption (PSA) unit or using membranes [22]) occur at high pressure and H_2 compression is extremely expensive from an energy point of view. This would involve the operation of CLR reactors under pressurized conditions, which is still unproven in circulating fluidized beds because the high pressure operation makes a stable circulation of solids and the loop seals rather challenging. A different approach for steam methane reforming have been proposed by Ryden et al. [23,24] in which the chemical looping reactor acts as combustion chamber to provide the heat of reaction to the reforming tubes which are immersed into the fuel reactor by converting the PSA-offgas into CO_2/H_2O inside the fuel reactor. In the last years, packed bed reactors (PBRs) have also been proposed for chemical looping combustion [25–28]. Diglio et al. [29] developed a 1D reactor model to simulate multiple cycles of a 22 cm long reactor with 6 cm diameter and presented the results of the cyclic process, where the reduction gas is first completely oxidized (gas-solid reactions) and thereafter the reformed syngas is produced.

In the present paper, chemical looping reforming in packed-bed reactors is tested and compared from an experimental and numerical point of view. With respect to the previous works on CLR, in the present work the OC reduction and reforming are not carried out in the same conversion step, but two different phases are distinguished. The proof of concept has been achieved in a lab-scale packed-bed reactor (3 cm of internal diameter, ID, and 1.5 m of reactor length) using Ni supported on $CaAl_2O_4$ as OC. The experimental demonstration focuses on the oxygen carrier stability under repeated reduction/reforming/oxidation phases for >400 h. A detailed reactor model is also discussed, which includes the estimation of the reactor heat losses and is validated with the experimental results. Finally, a large-scale reactor is designed and modelled for full scale applications for H_2 and CH_3OH production plants with integrated CO_2 capture.

2. Description of the concept and process integration

A schematic diagram of the CLR process with PBRs is presented in Fig. 1. Three main phases are carried out in sequence in three parallel reactors. The reactor operated in oxidation converts the Ni into NiO by reaction with the O_2 in the air stream while releasing N_2. The reactor operated in reduction, reduces the OC by using low grade fuel forming CO_2 and H_2O. Finally, a third reactor, in which the OC is in Ni form, is fed with natural gas together with recirculated CO_2/H_2O from the reduction phase and additional steam to convert CH_4 into syngas. The combination of CO_2/H_2O recirculation and additional H_2O is required to lower the H_2O consumption of the plant while keeping a very high CH_4 to H_2 conversion: in case only CO_2 is used, the reformate syngas is rich in CO and therefore more H_2O is required for the WGS reactions downstream of the CLR reactors; in case only H_2O (from the steam cycle) is used, relatively large quantities of H_2O are required to enhance the CH_4 conversion. Each reactor is operated sequentially in oxidation/reduction/reforming by switching the inlet gas streams. In order to avoid undesired mixing of the different reactants, a short purge cycle can be added before and after the oxidation.

In Fig. 2, a simplified plant flowsheet is depicted, illustrating a proposed process integration. After the reforming, the resulting syngas is cooled down to the desired temperature and sent to downstream plant units. In case of H_2 production, one or two conventional WGS

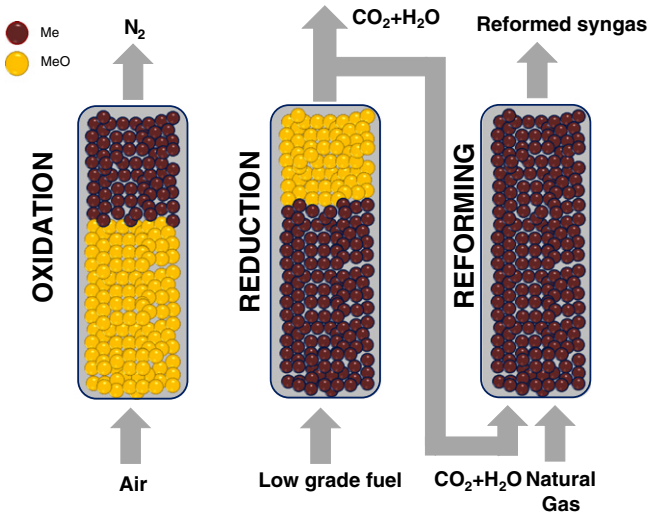

Fig. 1. Schematic of the CLR concept with PBR.

stages are required, depending on the CO content after the reforming. As discussed by Ryden et al. [23], complete CH_4 and CO conversion to H_2 is not strictly required because the PSA off-gas will be used in the reactor operated for the reduction. After the WGS reactors, a conventional state-of-the-art PSA process is used to meet the required H_2 purity. In case of CH_3OH production, the reformate is compressed to the operating pressure for the methanol synthesis (up to 50–100 bar) and is converted into a CH_3OH-rich stream. Part of the incondensable gases from the methanol separation unit is sent back to the CH_3OH converter and the remaining part is used for the reduction of the OC. The air flow rate to the reactor operated in oxidation is compressed to the CLR operating pressure and the remaining N_2 is then expanded in a gas turbine, reducing the electricity demand of the plant.

With respect to conventional FTR plants, the PBR CLR process does not require an external furnace and high temperature heat transfer surface because the process is auto-thermal. Compared to ATR, no ASU is needed to produce high purity oxygen and avoid syngas dilution with N_2. With respect to the dual fluidized bed CLR, the proposed PB process maintains the high hydrogen production efficiency and can be operated at higher pressure. Moreover, intrinsic CO_2 separation is achieved in the PB CLR process, which delivers a high pressure CO_2 stream without the need of a dedicated process based on amines or on more advanced technologies.

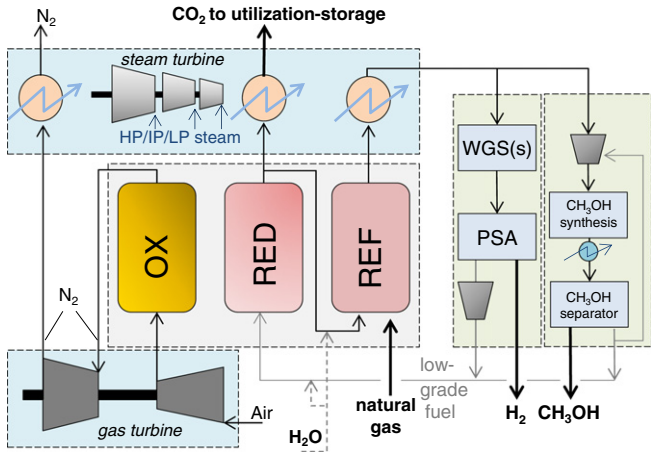

Fig. 2. Layout of the integrated CLR PB process for H_2 and CH_3OH production with integrated CO_2 capture.

With respect to the integrated reformer with CLC and all the other mentioned alternative technologies, the steam consumption can be reduced thanks to the CO_2/H_2O recirculation. A higher H_2 production efficiency is also expected because the oxidation and reduction phases are carried out at lower temperatures, reducing the overall heat duty required for the process.

On the other hand, high temperature packed-bed processes are characterized by intrinsic dynamic behavior and thus require a proper heat management strategy, as will be discussed in the following sections.

3. Description of the experimental facilities

The experimental validation of CLR with PBR has been carried out in an existing facility at the Eindhoven University of Technology (TU/e). As shown in Fig. 3, it consists of a high temperature resistant stainless steel tube (ODxIDxL = 36 × 30 × 1500 mm), with 48 access points for the insertion of thermocouples (Rössel, type K). With this configuration, unsteady axial temperature profiles can be measured with good spatial resolution in the middle of the bed with a temporal resolution of 1 Hz. The reactor is surrounded in all its length by three electrical furnaces, which allow imposing a uniform initial temperature profile in the section where the active material is present. Finally, in order to limit the heat losses towards the environment, the reactor was placed in a box filled with insulating material (glass wool). The setup has been used in the past for model validation and for a heat management investigation of CLC in dynamically operated packed-bed reactors [30,31]. The feed flow rate and composition is controlled by Bronkhorst mass flow controllers. The reactor exhaust stream is cooled with a water cooler. The dry gas composition can be measured during all the stages of the experimental procedure using a mass spectrometer (Cirrus 2, MKS Instruments). In order to distinguish CO and N_2 fractions in the gas, an additional CO analyzer was used (ULTRAMAT 23 Gas Analyzer, Siemens). The inert material at beginning of the reactor is used in order to heat-up the inlet gas to the reaction temperature.

4. Description of the model

The model used for the present investigation is based on a 1D adiabatic axially dispersed packed bed reactor model, as presented in the following sections. The main assumptions are: i) radial velocity, temperature and concentration gradients are neglected; ii) The axial gas and solid temperature profiles are considered the same (pseudo-homogeneous model). The governing equations of the mass and energy balances for the reactor model together with the constitutive equations for the description of heat and mass dispersion are reported below. In the mass balances, the source terms consist of a summation over all the heterogeneously catalyzed gas phase reactions as well as gas-solid reactions. The numerical solution of the 1D reactor model is based on a finite difference discretization technique with higher order temporal and spatial discretization with local grid and time step adaption [32].

Gas phase balance

$$\varepsilon_g \rho_g \frac{\partial y_{g,i}}{\partial t} = -\rho_g v_g \frac{\partial y_{g,i}}{\partial x} + \frac{\partial}{\partial x} \rho_g D_{ax} \frac{\partial y_{g,i}}{\partial x} + \varepsilon_g \sum_k r_{k,i} MW_i \quad (6)$$

Solid phase balance

$$\varepsilon_s \rho_s y^0_{act} \frac{\partial y_{s,j}}{\partial t} = -\varepsilon_g \sum_k r_{k,j} MW_j \quad (7)$$

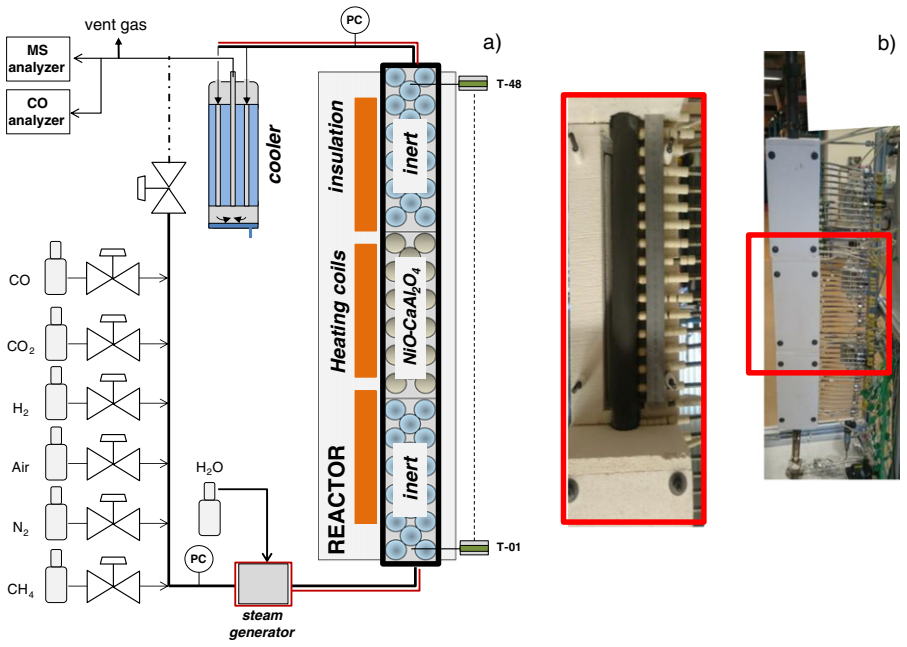

Fig. 3. a) Simplified schematic overview of the packed-bed reactor setup [30,31]. b) Pictures of the reactor.

Energy balance

$$\%\left(\varepsilon_g\rho_g C_{p,g}+\varepsilon_s\rho_s C_{p,s}\right)\frac{\partial T}{\partial t}=-\rho_g v_g C_{p,g}\frac{\partial T}{\partial x}+\frac{\partial}{\partial x}\lambda_{ax}\frac{\partial T}{\partial x}+\varepsilon_g r_i\Delta H_{R,i}+\alpha_{ext}\frac{4}{d_{ext}}\left(T_w-T_{ext}\right) \quad (8)$$

Effective axial heat dispersion [33]

$$\lambda_{ax}=\lambda_{bed,0}+\frac{RePr\lambda_g}{Pe_{ax}}+\frac{Re^2Pr^2\lambda_g}{6(1-\varepsilon_g)Nu} \quad (9)$$

Heat Péclet axial number [34]

$$Pe_{h,ax}=\frac{2\left(0.17+0.33\,,\exp\left[\frac{-24}{Re}\right]\right)}{1-\left(0.17+0.33\,,\exp\left[\frac{-24}{Re}\right]\right)} \quad (10)$$

Nusselt Number [35]

$$Nu=\left(7-10\varepsilon_g+5\varepsilon_g{}^2\right)\left(1+0.7Re^{0.2}Pr^{1/3}\right)+\left(1.33-2.4\varepsilon_g+1.2\varepsilon_g{}^2\right)Re^{0.7}Pr^{1/3} \quad (11)$$

Axial mass dispersion [36]

$$D_{ax}=\left(\frac{0.73}{Re\;Sc}+\frac{0.5}{\varepsilon_g+\frac{9.7\varepsilon_g{}^2}{Re\;Sc}}\right)v_g d_p \quad (12)$$

4.1. Reaction kinetics

The particle properties used in the model have been measured by means of a pycnometer (Quantachrome Micro-ultrapyc1200) and BET measurements (with Thermo-scientific Surfer) and are reported in Table 1.

The kinetics of Ni oxidation and NiO reduction have been determined with thermogravimetric analysis (TGA) by Medrano et al. [37] and the obtained parameters are listed in Table 2. No kinetic parameters are indicated for the reduction with CH_4, because it was observed that when methane was used for the reduction of NiO, the oxygen carrier did not show any activity when the OC was fully oxidized, while reduction was observed when the sample was already partially reduced. This can be easily explained by recalling that Ni is a good catalyst for steam methane reforming, which occurs before the reduction reaction when CH_4 is fed. The reforming reaction produces H_2 and CO, which are subsequently responsible for the complete reduction of the oxygen carrier.

$$\frac{1}{2}O_2+Ni\rightarrow NiO \qquad \Delta H_0{}^{298K}=-479.4kJ/mol_{O_2} \quad (13)$$

$$H_2+NiO\rightarrow H_2O+Ni \qquad \Delta H_0{}^{298K}=-2.125kJ/mol_{H_2} \quad (14)$$

$$CO+NiO\rightarrow CO_2+Ni \qquad \Delta H_0{}^{298K}=-43.26kJ/mol_{CO} \quad (15)$$

$$r_{Ni}\left[\frac{mol}{m_p^3 s}\right]=\frac{\varepsilon_{s.p}\rho_s y^0_{act}}{b\cdot MW_j}\frac{dX_j}{dt} \quad (16)$$

Table 1
Particle Properties of $NiO/CaAl_2O_4$ for particle model [37].

Oxygen carrier	17–18.5 wt% NiO on $CaAl_2O_4$
Particle diameter [mm]	1 ÷ 1.7
Particle porosity [$m^3{}_g\,m^{-3}{}_p$]	0.55
Average pore size [Å]	130
Tortuosity	2

Table 2
Kinetic parameters for the reduction and oxidation of $Ni/NiO/CaAl_2O_4$ particles, taken from [37].

	H_2	CO	O_2
C_S [mol m^{-3}]	89,960	89,960	151,200
r_0 [m]	$3.13\cdot10^{-8}$	$3.13\cdot10^{-8}$	$5.8\cdot10^{-7}$
k_0 [$mol^{1-n}\,m^{3n-2}\,s^{-1}\,bar^q$]	$9.0\cdot10^{-4}$	$3.5\cdot10^{-3}$	$1.2\cdot10^{-3}$
E_A [kJ mol^{-1}]	30	45	7
n	0.6	0.65	0.9
D_0 [$mol^{1-n}\,m^{3n-1}\,s^{-1}$]	$1.7\cdot10^{-3}$	$7.4\cdot10^{6}$	1
E_D [kJ mol^{-1}]	150	300	0
k_x	5	15	0
b	1	1	2

Table 3
Fitted kinetic parameters for SMR and WGS for the $Ni/CaAl_2O_4$ oxygen carrier.

	$k_{0,i}$	$E_{A,i}$
$k_{SMR}\left(\frac{mol}{s \cdot kg_{cat} bar^{0.404}}\right)$	$3.65 \cdot 10^2$	42.8
$k_{WGS}\left(\frac{mol}{s \cdot kg_{cat} bar}\right)$	$2.45 \cdot 10^2$	54.5

$$\frac{dX_j}{dt} = \frac{\frac{3C_g^n}{b \cdot r_0 \cdot C_s}}{\left(\frac{1}{k}(1-X)^{-\frac{2}{3}} + \frac{r_0}{D}\left((1-X)^{-\frac{1}{3}} - \frac{r_0}{D}\right)\right)} \quad (17)$$

$$k = k_0 \exp\left(\frac{-E_A}{RT}\right) \quad (18)$$

$$D = D_0 \exp\left(\frac{-E_D}{RT}\right) \exp(-k_x X) \quad (19)$$

The Ni-based oxygen carrier also works as catalyst for the reforming and shift reactions. The expressions used to model the reforming and water gas shift reaction kinetics (given in Eqs. (20)-(22)) were taken from Numaguchi and Kikuchi [38] and the parameters were fitted to experimental data for the oxygen carrier, since Medrano et al. have shown that the kinetic model of Numaguchi and Kikuchi over-predicts the conversion rates for this oxygen carrier [37]. The fitted kinetic parameters for SMR and WGS have listed in Table 3. This model does not consider the dry reforming reaction (i.e. reforming by CO_2), so to simulate this case, the model was operated assuming an initial H_2O partial pressure equal to 10^{-6}, which was sufficient to avoid numerical issues, since the steam reforming is faster than the dry reforming [39].

$$r_{SMR} = \frac{k_{SMR}\left(p_{CH_4} p_{H_2O} - p_{H_2}^3 p_{CO}/K_{SMR}\right)}{p_{H_2O}^{1.596}} \quad (20)$$

$$r_{WGS} = \frac{k_{WGS}\left(p_{CO} p_{H_2O} - p_{H_2} p_{CO_2}/K_{WGS}\right)}{p_{H_2O}} \quad (21)$$

$$k_i = k_{0,i} \exp\left(\frac{-E_{A,i}}{RT}\right) \varepsilon_{s,p} \rho_s \omega_{Ni} \quad (22)$$

4.2. Radial heat losses

A detailed thermal model for the prediction of radial heat losses (see Eq. (8)) has been included in this work, considering the thermal resistances illustrated in Fig. 4. To determine the overall radial heat transfer coefficient α for the reactor used in this experimental work, two different sections need to be considered: the first section is from the center of the reactor - where the temperature is measured - to the reactor wall and the second section considers the heat exchange from the reactor wall to the heaters, where three thermocouples are located to control the temperature. The equations used to determine the partial

Table 4
Equations used for the thermal model to describe the radial heat losses.

Overall heat exchange coefficient α [W/m²/K]	$\alpha_{PB} = \frac{(R_{CF} + R_{FS} + R_{FW})(R_{CS} + R_{SW})}{R_{CF} + R_{FS} + R_{FW} + R_{CS} + R_{SW}} + R_{steel}$ (23)
	$\alpha_{ext} = \frac{R_{air} R_{rad}}{R_{air} + R_{rad}}$ (24)
	$R_{steel} = \frac{, \ln(d_{ext,react}/d_{int,react})}{2\pi L \lambda_{steel}}; R_{air} = \frac{, \ln(d_{oven}/d_{ext,react})}{2\pi H \lambda_{air}}$ (25)
Radial resistance (inside the reactor) [40,41]	$R_{CF} = \frac{0.5 d_{int,react}}{4\lambda_g}; R_{CS} = \frac{0.5 d_{int,react}}{4\lambda_s}; R_{FS} = \frac{d_p}{Nu_{fs}\lambda_g};$ $R_{FW} = \frac{d_p}{Nu_{fw}\lambda_g}; R_{SW} = \frac{1}{h_{sw}} = \frac{1}{2.12}\frac{d_p}{\lambda_{rs}}$ (26)
Radiation from the oven	$R_{rad} = \frac{\sigma A_{wall}}{\left(\frac{1-\varepsilon_{steel}}{\varepsilon_{steel}} + \frac{A_{oven}}{A_{wall}} + \frac{1-\varepsilon_{oven}}{\varepsilon_{oven}}\frac{A_{wall}}{A_{oven}}\right)} (T_{oven}^2 + T_{wall}^2)(T_{oven} + T_{wall})$ (27)
Gunn equation (1978) [35]	$Nu_{fs} = \left(7 - 10\varepsilon_g + 5\varepsilon_g^2\right)\left(1 + 0.7 Re^{0.2} Pr^{1/3}\right) + \left(1.33 - 2.4\varepsilon_g + 1.2\varepsilon_g^2\right) Re^{0.7} Pr^{1/3}$ (28)
Yagi and Wakao (1959) [42]	$Nu_{fw} = 0.6 Re^{0.5} Pr^{1/3}$ (29)
Stagnant bed conductivity (Zehner and Schlünder, 1970) [43]	$\%\frac{\lambda_{rs}}{\lambda_g} = \sqrt{1-\varepsilon_g}\left(\frac{\lambda^0}{\lambda_g}\right)$ $\frac{\lambda_{bed,0}}{\lambda_g} = \frac{2}{\left(1 - \frac{\lambda_g B}{\lambda_s}\right)}\left[\frac{\left(1 - \frac{\lambda_g}{\lambda_s}\right)B}{\left(1 - \frac{\lambda_g B}{\lambda_s}\right)^2}, \ln\left(\frac{\lambda_s}{\lambda_g B}\right) - \frac{B+1}{2} - \frac{B-1}{\left(1 - \frac{\lambda_g B}{\lambda_s}\right)}\right]$ $B = 1.25\left(\frac{1-\varepsilon_g}{\varepsilon_g}\right)^{10/9}$ (30)

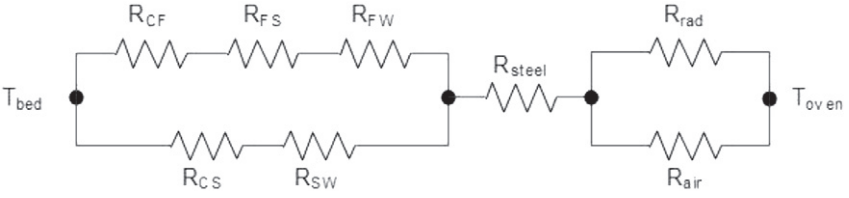

R_{CF}	Conductive resistance from the center of the bed to the fluid phase	R_{FS}	Resistance from the fluid phase to the solid phase
R_{FW}	Resistance from the fluid phase to the reactor wall	R_{CS}	Conductive resistance from the center of the bed to solid phase
R_{SW}	Resistance from the solid phase to the reactor wall	R_{steel}	Resistance to conduction in the reactor thickness
R_{rad}	Resistance to radiation between the reactor and the oven	R_{air}	Resistance to conduction between the reactor and the oven

Fig. 4. Representation of the overall heat transfer coefficient by means of thermal resistances.

Fig. 5. OC/catalyst (left) and inert material (right) used in the reactor for the experiments.

heat transfer resistances were taken from the studies by Dixon and Cresswell on the thermal conductivity of packed beds [40,41] and have been summarized in Table 4 (Eqs. (23)-(30)).

5. Model validation

The reduction and oxidation phases of the chemical looping reforming process with packed-bed reactors are substantially similar to those for the PB-CLC [25,26,30,44]. The main novelty in this process is represented by the heat removal step, which is carried out by means of an endothermic reaction instead of blowing air or nitrogen through the reactor as in the case of CLC.

The reactor has been filled with inert material (Fig. 5, right) at the beginning and at the end of the reactor (upstream and downstream of the catalyst bed) in order to ensure a complete pre-heating of the gas to the desired reaction temperature (as shown in Fig. 3a). In the middle of the bed, 500 g of a Ni-based oxygen carrier supported on $CaAl_2O_4$ (Table 1) shown in Fig. 5 (left) has been placed, which corresponds to about 0.5 m of reactor length.

In order to check the stability of the OC in terms of oxygen transfer capacity and redox reactivity, a stream consisting of 20% H_2 and 20% H_2O (balance N_2) has been used for the reduction phase after oxidation with air and the hydrogen breakthrough has been recorded (Fig. 6). As can be seen, except for the first few redox cycles when the material was still being activated, the H_2 breakthrough curves are practically overlapping even up to 300 h of operation indicating complete and stable activation.

The stability of the OC used for this experiment has been confirmed also by Medrano et al. [37] through tests with >200 redox cycles in a TGA apparatus. The stability of the Ni-based OC under repeated cycles in a medium scale reactor setup confirms that the scale-up of a Ni-based oxygen carrier supported on $CaAl_2O_4$ is promising for demonstration at pre-commercial and commercial scales in the near future.

All the experiments were carried out using N_2 during the heating up of the system and in between two different experiments in order to ensure that the temperature was kept constant along the reactor and no traces of reactants were left inside the reactor before commencing the experiments.

5.1. Oxidation

The oxidation phase was carried out using 9 NL/min of air. The theoretical temperature rise at the reaction front (Noorman et al. [44] and Fernandez et al. [45]), with 18% (wt. fraction) of Ni is about 700 °C and therefore the initial bed temperature has been set to 400 °C to avoid excessive overheating of the system.

The breakthrough of the oxygen starts after 100 s and concludes after about 5 min. Fig. 7 shows the O_2 fraction at the outlet section. The model predicts with reasonable accuracy the shape of the breakthrough curve. The time required for complete oxidation corresponds with the one predicted based on the amount of oxygen fed to the reactor and the overall oxygen capacity of the OC. The small discrepancy between the model prediction and the experimental results is explained by radial gradients caused by heat losses resulting in a slightly inhomogeneous gas distribution along the radial direction. Another important reason of the larger mass dispersion in the experiments is related to the long piping and the large volume of the gas cooling system downstream the reactor unit before the analyzer. Both effects were not accounted for in the reactor model (the interested reader is referred

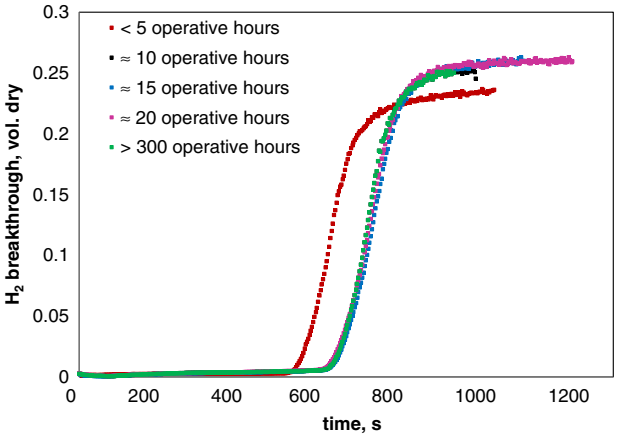

Fig. 6. H_2 breakthrough during the stability test (using 10 NL/min of 20% H_2, 20% H_2O, 60% N_2) at 900 °C.

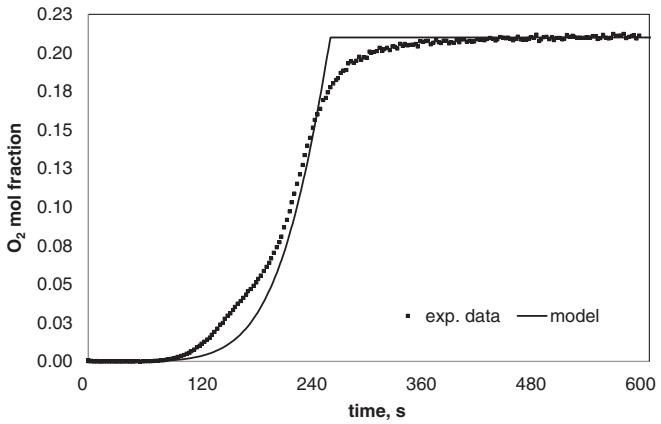

Fig. 7. O_2 molar fraction at the reactor outlet as a function of time during the oxidation cycle starting with solid temperature at 400 °C.

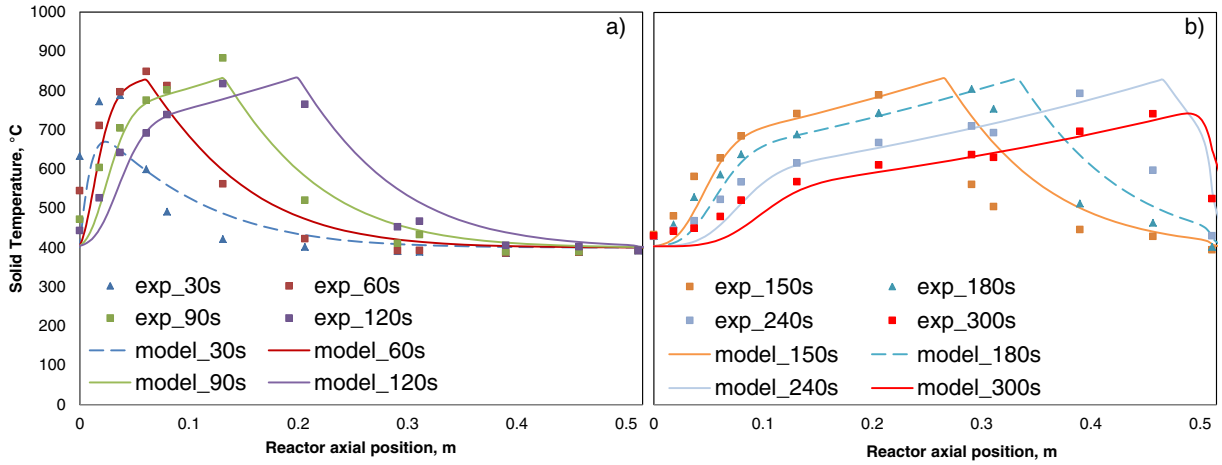

Fig. 8. Axial solid temperature profiles at different times during the oxidation phase: a) from 0 to 120 s and b) from 150 ro 300 s. (10 NL/min of air with solid temperature at 400 °C).

to the attached supplementary material for a more detailed discussion on this).

Fig. 8 presents the axial temperature profile in the bed at different instances during the oxidation phase, and shows that the reaction front propagates along the bed until it reaches the end of the reactive zone at around 300 s. The solid reactor is cooled by flowing N_2 through the reactor for >1 h and setting the heating coils to 400 °C as set point temperature Also the heat front propagates through the bed, but with a lower velocity, so that the heat front remains at around 0.1 m from the inlet section after 300 s. The figure also clearly shows, especially for the longer times shown in Fig. 8b, that the temperature is higher in the last part of the bed and that the temperature plateau is not flat, as expected by theoretical descriptions of adiabatic packed-bed CLC reactors [46]. The reason for this behavior is the presence of radial heat losses, related to the set point temperature of the heating coils at 400 °C. Therefore, once the reaction front has passed, the bed cools down. The cooling of the bed due to radial heat losses is well captured by the model, confirming the accuracy of the description of the radial heat losses in the developed model.

The reaction front is clearly visible in both the experiments and modelling results. At the beginning of the oxidation phase, the results from the model and the experiments match very well. After 150 s (Fig. 8b), the results from the model predict a slightly higher reaction front velocity, so that the discrepancy with the experimental results increases somewhat. As already discussed by Hamers et al. [30] for the oxidation with a Cu-based oxygen carrier, one of the reasons of this difference is related to the description of internal diffusion limitations inside the relatively large particles, which is not fully captured by the selected redox kinetics.

5.2. Reduction

The reduction of the OC has been carried out after heating the bed to 800 °C or 900 °C and by keeping the set point temperature of the heating coils at the same values. As shown in Fig. 9a, for the indicated flow rate and composition of the reacting gas, the breakthrough of CO and H_2 was detected after about 5 min and lasted until 10 min, when a constant gas composition was reached. With respect to the reduction reactions, the model predicts the breakthrough time correctly, although the breakthrough curves predicted by the model (Fig. 9a) are much steeper than the ones obtained from the experiments, as also shown for the oxidation breakthrough curves. This is again mainly due to the mass dispersion, which is amplified in this case due to the lower gas flow rate (due to the water condensation in the cooler) and the lower molecular weight of the gas (below 20 kg/kmol). It can be noted that the final outlet composition does not correspond to the syngas feed, because the oxygen carrier is active for the water-gas-shift reaction (in this case the reverse WGS), thus resulting in a lower amount of H_2 and CO_2 and a higher amount of CO. Due to the low heat of reaction associated with the reduction of NiO with CO/H_2-rich syngas, the axial solid temperature profile does not significantly change during the reforming step, as shown in Fig. 9b. The reduction tests at 800 °C showed a similar

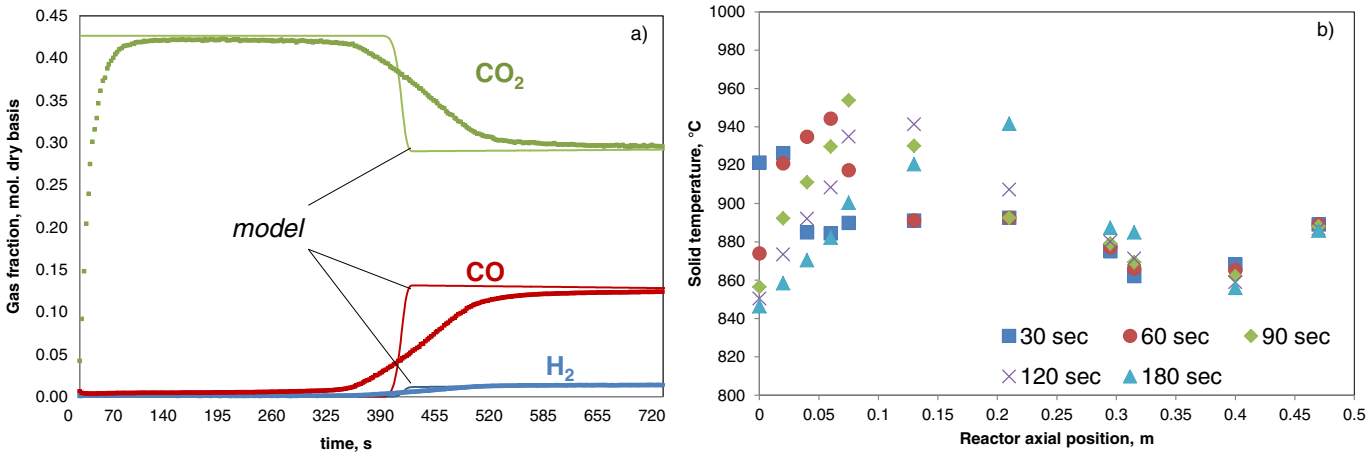

Fig. 9. a) Gas composition at the reactor outlet during the reduction phase at 900 °C using 10 NL/min of a gas mixture with CO 10%, H_2 10%, CO_2 30% (balance with N_2); b) Axial solid temperature profile at different instances during the reduction phase.

behavior. The main difference is in the gas composition after the complete breakthrough, in which the amount of H_2 and CO_2 is higher due to the different equilibrium constant for WGS at lower temperatures.

5.3. Reforming

During the reforming phase, the syngas is fed to the system and only catalytic reactions take place because the OC was completely reduced to Ni during the preceding reduction phase. Two different feed gas compositions have been tested corresponding to steam and dry reforming cases respectively, with an inlet gas flow rate of 20 NL/min and an initial bed temperature of about 800 °C or 900 °C (Table 5). After the reactor has reached its set-point temperature, a CH_4-rich gas has been fed to the system while the heating system was switched off in order to avoid an energy influx to the reactor from the external heating coils. The reforming reaction was continued until the temperature in the oven had decreased about 10–20 °C (corresponding to about 5 min). In this way, it is possible to compare the experimental and modelling results assuming a constant temperature in the oven without heating power from the heating coils. This was not required during the exothermic oxidation and reduction phases.

The gas compositions at the reactor outlet as a function of time are shown in Fig. 10. The results from the model (solid lines) are in good agreement with the experiments (markers). The measured compositions are always at the chemical equilibrium, confirming that the reforming of methane is an equilibrium controlled reaction. The difference between the model and experimental results was always in the range ±1%, after sufficient time on stream during the testing period. At the beginning of the experiments, the CO content is somewhat higher, however, after some time (about 1 min), the final equilibrium composition is reached.

In Fig. 11, the axial solid temperature profiles at different instances during the reforming phase are shown. A decrease in the temperature at the beginning of the bed where the CH_4 with H_2O/CO_2 is reacting with the catalyst can be clearly discerned. The solid temperature decreases by >200 °C at the inlet, while it maintains at the initial temperature towards the outlet section after syngas has reached its equilibrium composition. As expected, the temperature decrease is higher for the dry reforming cases, related to about 20% higher reaction enthalpy of dry reforming relative to steam reforming. The experiments show clearly how the bed is progressively cooled due to the reforming reactions. At the beginning, the syngas contacts the hot solid/catalyst in the first part of the bed, the reforming reactions take place and the temperature decreases. After that, the $CH_4 + CO_2/H_2O$ is partially converted in the first part of the bed (first 10 cm) due to the lower temperature of reaction and the conversion is completed in the second part of the reactor where the solid/catalyst is at higher temperature. The zone at lower temperature in the reactor increases with reaction time, which indicates the possibilities for effective indirect heat transfer from the oxidation phase to the reforming phase.

Table 5
Operating conditions for the reforming phase tests.

Reforming conditions		
Initial bed temperature, °C	800/900	
Inlet gas flow rate, NL/min	20	
Inlet pressure, bar	1.1	
Inlet gas composition, %vol.		
CH_4	5	5
CO_2	–	30
H_2O	30	–
N_2	65	65

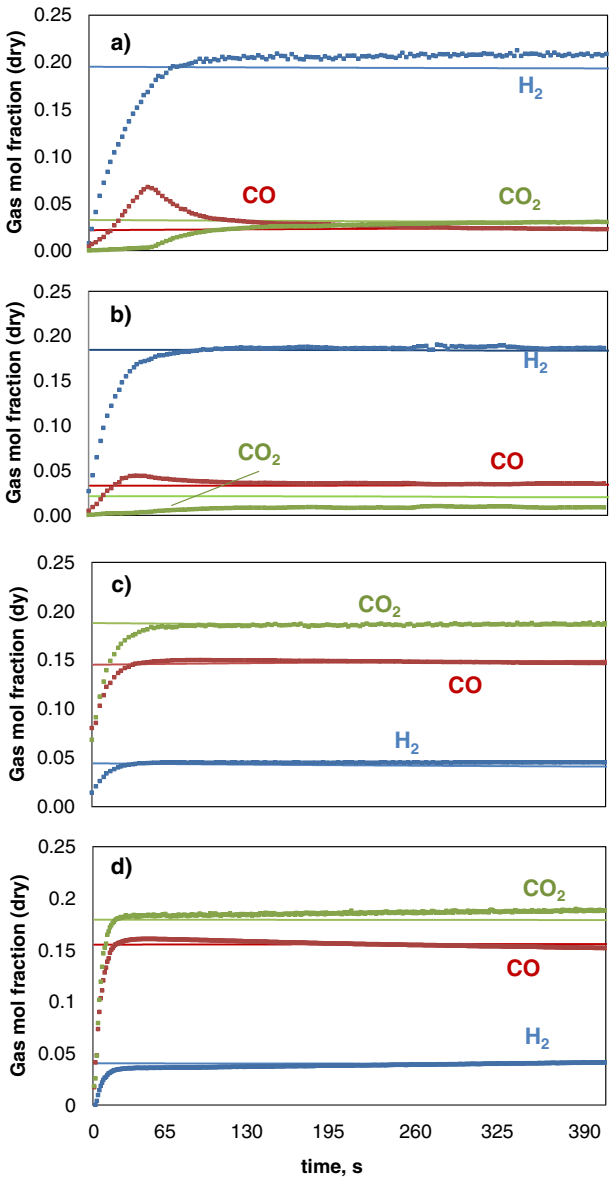

Fig. 10. Gas composition at the reactor outlet during the reforming phase with the gas compositions reported in Table 5 for steam reforming (case a and b) and dry reforming (case c and d) at 800 °C (case a and c) and 900 °C (case b and d).

6. Reactor design and heat management

Using the 1D reactor model previously described and validated at lab-scale, the design and heat management of an industrial-scale chemical looping reforming reactor system have been carried out for integration in both H_2 and CH_3OH plants. The size of the reactors is based on commercial large-scale plants. Based on preliminary mass and energy balances of the integrated plants shown in Fig. 2, the corresponding flow rates, temperatures and gas compositions have been estimated in order to obtain a syngas with the required specifications for the downstream units. Subsequently, the 1D model was run for multiple cycles of the reduction/reforming/oxidation phases in sequence, where it was assumed that the reactor was purged with pure N_2 for a short period after the reforming and oxidation phases in order to remove any reactive gases inside the reactor and avoid the formation of explosive mixtures. The dynamically operated adiabatic PBRs have been simulated for a complete cycle with the inlet gas conditions for the different phases listed in Table 6.

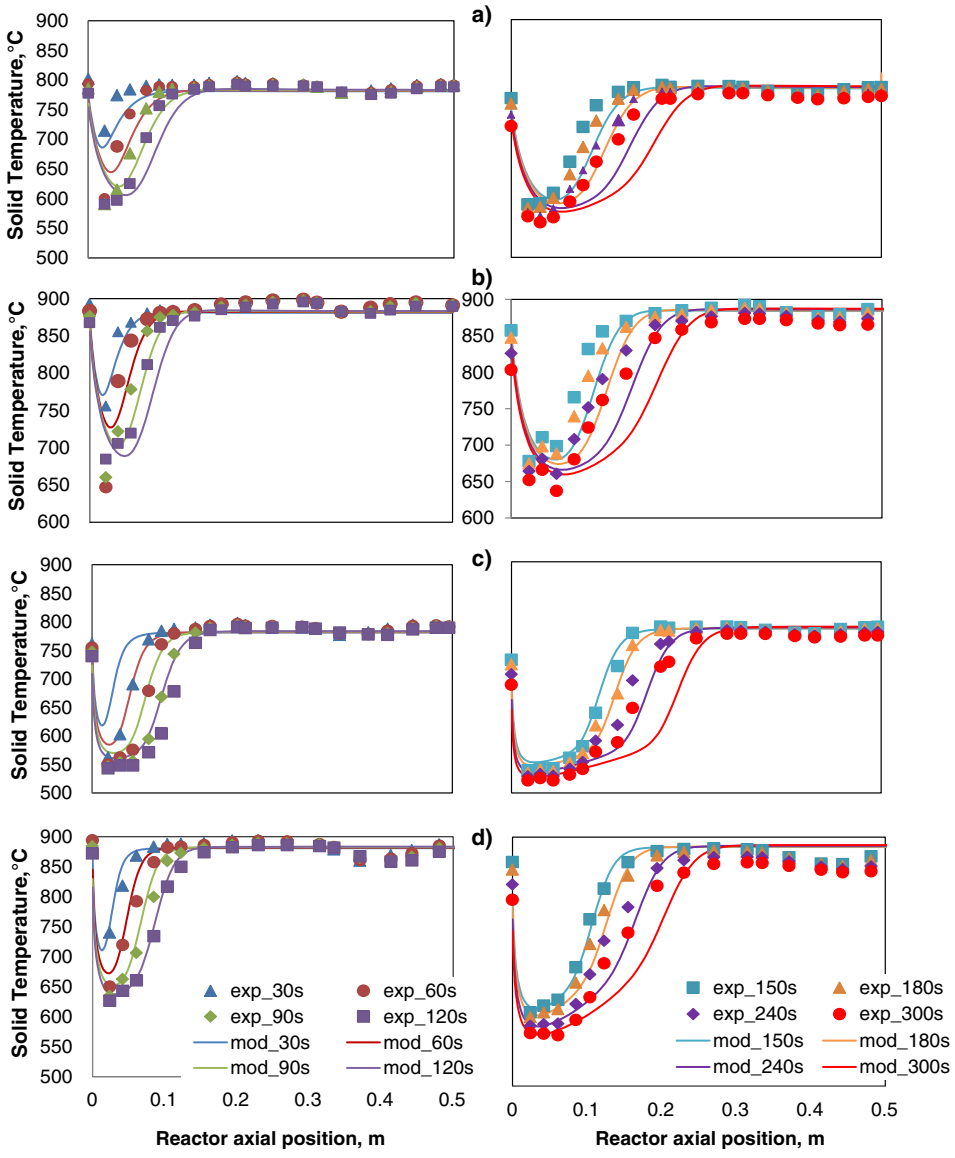

Fig. 11. Axial solid temperature profiles at different instances during the reforming phase at 800 °C with the gas compositions reported in Table 5 for steam reforming (case a and b) and dry reforming (case c and d) at 800 °C (case a and c) and 900 °C (case b and d).

Compared to the results presented in the previous part of the manuscript where the model was validated, the operating conditions and the heat management strategies are different. In particular: there is no external electric furnace considered to stabilize the reactor temperature, therefore no thermal interaction occurs with the external environment resulting in an overall adiabatic process; the solid temperature profile at the end of each phase is the initial temperature profile of the following phase; the gas inlet temperature and pressure are resulting from the complete process.

For fixed WGS and PSA operating conditions, the conditions obtained are the optimal (or very close to it) to achieve high H_2 yield. A different optimization is needed when also the contributions of electricity and steam are considered and it will be carried out in a dedicated techno-economic assessment.

The results presented in this section have been obtained after running the model for multiple cycles to reach a cyclic steady-state. To determine whether the cyclic steady-state was attained the temperature, flow rate and gas compositions at the reactor outlet, as well as the axial solid conversion and temperature profiles were compared for two consecutive cycles.

The following overall energy balance of the process is considered for the current system.

Adiabatic conditions
$$H_{in} = H_{out} \tag{31}$$

Energy at the inlet
$$\left(\dot{m}_{ox}h_{ox}(T,x)\Delta t_{ox} + \dot{m}_{red}h_{red}(T,x)\Delta t_{red} + \dot{m}_{ref}h_{ref}(T,x)\Delta t_{ref} + 2\dot{m}_{purge}h_{purge}(T,x)\Delta t_{purge}\right)_{inlet} = H_{in} \tag{32}$$

Energy at the outlet
$$\left(\int_{t_{ox}} \dot{m}_{ox}h_{ox}(T,x)dt + \int_{t_{red}} \dot{m}_{red}h_{red}(T,x)dt + \int_{t_{ref}} \dot{m}_{ref}h_{ref}(T,x)dt + 2\int_{t_{purge}} \dot{m}_{purge}h_{purge}(T,x)dt\right)_{outlet} = H_{out} \tag{33}$$

Where Δt_i is the total phase time and the conditions of the streams at the inlet are constant, while at the outlet the conditions vary with the time generating a profile. In fact the energy associated to the gas at inlet is only dependent on the temperature and the gas composition,

Table 6
Operating conditions used to simulate a large-scale PB-CLR reactor system for H_2 or CH_3OH production.

	Hydrogen plant				Methanol plant			
	Reduction	Reforming	Oxidation	Purge	Reduction	Reforming	Oxidation	Purge
Reactor								
Diameter, m		3.5				3.5		
Length, m		10.5				10.5		
Void fraction, m^3 gas/m^3 r		0.5				0.5		
Oxygen carrier								
Ni content (on $CaAl_2O_4$), %wt		8				8		
Particle diameter, mm		2				2		
Gas inlet conditions								
Temperature, °C	600	600	600	600	600	600	600	600
Pressure, bar	20	20	20	20	20	20	20	20
Flow rate, kg/s	12.67	16.356	16.244	4.8	12.51	27.7	34.2	9.8
Composition, %vol.								
CH_4	2.5	22.3	–	–	4.6	26.4	–	–
CO	14.3	0.0	–	–	3.7	–	–	–
CO_2	53.9	22.3	–	–	10.0	7.9	–	–
H_2O	–	55.4	–	–	44.9	65.7	–	–
H_2	29.3	–	–	–	36.7	–	–	–
N_2	–	–	79	100	–	–	79	100
O_2	–	–	21	–	–	–	21	–
MW, kg/kmol	27.0	23.4	28.9	28.0	15	19.5	28.9	28.0
Phase time, sec	600	600	600	60	275	275	275	25

while the outlet mass flowrate, temperature and gas composition change according to the dynamic operations of the reactor. It must be noticed that these equations are needed to avoid any accumulation (or losses) of energy every complete cycle.

The design and operating conditions of the PBRs for the H_2 and CH_3OH production plants have been reported in Table 6. The reactor diameter and length have been selected to assure a superficial gas velocity below 1 m/s for all the phases. The final geometry of the reactor should be further optimized via a techno-economic optimization, which is beyond the scope of this work.

In the next two sections the heat management of the packed-bed chemical looping reforming reactors is discussed for hydrogen and methanol production.

6.1. Heat management of PB-CLR process for H_2 production

The size of the plant is based on 30 kNm^3/h of pure H_2 production. The syngas produced in the chemical looping reforming reactor is sent to a WGS unit operated at 350 °C to convert the CO into CO_2 while increasing the H_2 production. Downstream of the WGS unit, pure H_2 is recovered with a PSA unit operated with a 75% hydrogen recovery factor. The PSA off-gas (mostly H_2 and CO_2 with some unconverted CO and CH_4) is compressed and sent to the reactor operated in the reduction phase. With this system a reforming efficiency of 81% corresponding to 2.74 mol_{H2}/mol_{CH4} can be achieved with a steam consumption of 2 $kmol_{H2O}/kmol_{CH4}$ and CH_4 conversion in the reforming phase above 92% while 100% CO_2 capture is accomplished. The composition of the reducing gas has been obtained by performing some preliminary process simulation in order to have enough syngas available for the reduction to avoid the use of fresh CH_4 at the reduction. The stream at the reduction can also be different, depending on the selected operating conditions of the entire system as discussed in [47].

The gas composition and the temperature at the reactor outlet during the different phases are shown in Fig. 12. During the reduction phase, full conversion of fuel to H_2O and CO_2 is reached, while the oxygen carrier is reduced to Ni. The composition of the PSA off-gas fed to the reduction phase (Table 6) has a high CO_2 content (>50%). This is beneficial for the system because the low CO + CH_4 content (about 15%) makes carbon deposition unlikely, eliminating the need for further dilution with H_2O. The temperature at the reactor outlet is almost constant (around 950 °C) which is positive for the downstream processes, such as the gas coolers for steam generation, which can be designed to be operated at steady state conditions.

During the reforming phase, the syngas reaches a stable composition after 10 s. The reformed syngas is at chemical equilibrium at the temperature of the outlet gas. For >90% of the time of the reforming phase, CH_4 is almost completely converted into H_2 and CO and sent to the downstream processes. Compared to a conventional FTR, two main differences can be noted. The first difference is related to the transient syngas conditions during the last 50 s (representing 10% of the complete reforming phase), where the gas temperature at the reactor outlet decreases and the CH_4 conversion reduces significantly. The second difference is the H_2/CO ratio in the reforming product gas stream, which is about 1.8 mol_{H2}/mol_{CO}, instead of 2.8 of conventional standalone FTR due to the large amount of CO_2 which is fed to the reforming step, originating from the recirculated CO_2/H_2O product stream during the reduction phase. The lower H_2 fraction may affect the cost of the PSA downstream which is working with a more diluted H_2 stream (≈60% on a dry basis instead of conventional 70%). Therefore a techno-economic optimization of the complete plant has to consider also the optimization of the PSA.

During the oxidation phase, the temperature slightly decreases from 750 °C to 680 °C and the Ni is oxidized to NiO. The oxidation phase is integrated with a gas turbine cycle with an uncooled turbine, where the oxidation phase off-gases (mostly N_2 with some Ar and traces of gases present in the air), are expanded to ambient pressure and released to the atmosphere. The gas turbine inlet temperature is much lower than the typical value of about 1200 °C of CLC processes for power generation. The gas turbine pressure ratio is also dictated by the operating conditions of the reforming phase, resulting in sub-optimal gas cycle parameters with lower efficiency and low specific work.

The axial temperature profiles at the end of the oxidation, reduction and reforming phases are shown in Fig. 13. At the end of the reforming phase, the bed temperature increases along the reactor from about 550 to 700 °C. After the oxidation phase, the reaction front reaches the end of the reactor, while the heat front has only moved from the inlet of the reactor to the first 10% of the bed length. The temperature rise during the oxidation phase is about 300 °C and at the end of the oxidation phase the maximum temperature of the bed of almost 1000 °C is reached. After oxidation, the reduction phase starts with the PSA off-gas as fuel. As in the case of CLC with CO/H_2 rich syngas using Fe-based OC, discussed by the authors in [48], the maximum temperature of the bed does not change significantly, due to the low heat of reaction.

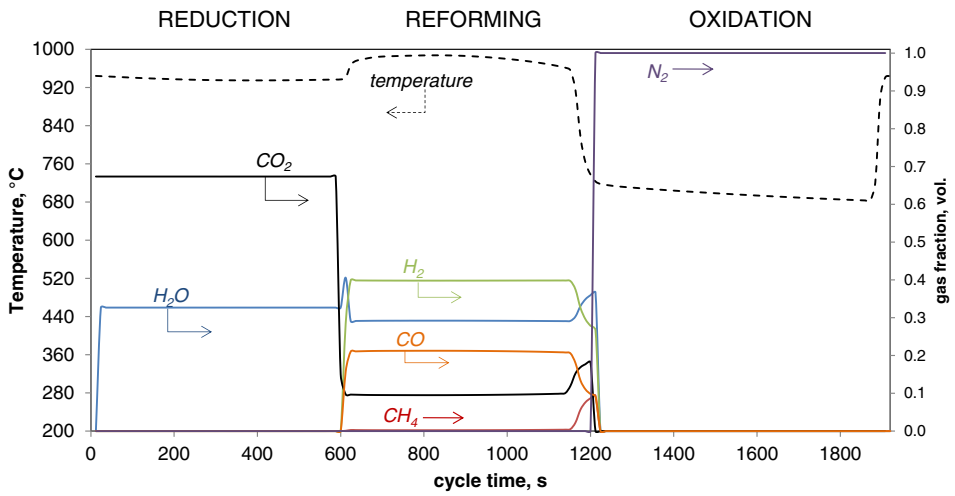

Fig. 12. Gas conditions (temperature and composition) at the reactor outlet during the consecutive reduction, reforming and oxidation phases for H_2 production (conditions listed in Table 6).

In this step, the heat front moves towards the end of the reactor, reaching 40% of the reactor length. Although the inlet temperature of the gas in the reduction phase is 600 °C, at the end of the reduction the bed temperature at the inlet is about 700 °C, because the composition of the inlet gas (rich in H_2 and CO/CO_2) favors the exothermic methanation reaction, for which the reduced Ni acts as catalyst. The syngas is therefore first converted into CH_4 achieving the equilibrium temperature and composition and then reformed where the solid is at higher temperatures. During the reforming phase the bed is cooled by two mechanisms: i) convective cooling by the gas flow, which moves the heat front to the reactor outlet blowing the heat out of the bed (similar to the PB-CLC heat removal phase); ii) cooling by the endothermic reforming reactions, which absorbs heat by converting the CH_4 into H_2 and CO. This second mechanism is a second heat front generated inside the reactor and it is due to the reforming reaction. It is more evident by comparing the axial temperature profile shown in Fig. 13 with the axial methane concentration profiles shown in Fig. 14. At the end of the reforming phase, the final bed temperature is reduced to 550–700 °C and the solids are ready to start a new oxidation cycle. Due to the bed cooling during the reforming, the solid temperature at the beginning of the oxidation is below 750 °C and therefore, the following oxidation delivers a gas with a low temperature (average 700 °C).

By inspecting the axial bed temperature profile shown in Fig. 13 and the axial CH_4 concentration profile in Fig. 14, one can discern that the CH_4 conversion occurs in two-stages: i) at the beginning of the bed, where the temperature is initially 700 °C and where the CH_4 vol. fraction reduces from the initial 22.5% to about 12% and ii) in the second part of the reactor, which is at high temperature, where the CH_4 is almost completely reformed. The thermal separation of these two reforming zones behaves like a combination of pre-reforming and reforming in a conventional FTR and the boundary between the two zones becomes smoother at the end of the reforming phase.

6.2. Heat management of the PB-CLR process for CH_3OH production

To investigate the heat management for the case of CH_3OH production, a plant of 5000 MTPD has been selected. Compared with the H_2 production unit, this plant is >200 times bigger, therefore 5 parallel lines of reduction, reforming and oxidation are considered to accommodate the larger amount of syngas required. Based on preliminary simplified calculations of the methanol synthesis process, the proposed system can achieve a CH_3OH yield of 0.9 mol_{CH3OH}/mol_{CH4} which compares very favorable with the performance of a state-of-the-art CH_3OH plant (0.82 mol_{CH3OH}/mol_{CH4}) [10]. Overall, 2 $kmol_{H2O}/kmol_{CH4}$ is consumed during the reduction and reforming phases. The carbon species which are not converted into CH_3OH in the synthesis unit are purged and are used as fuel for the reduction step, where they are converted into CO_2, which is compressed and stored after the gas cooling and H_2O separation.

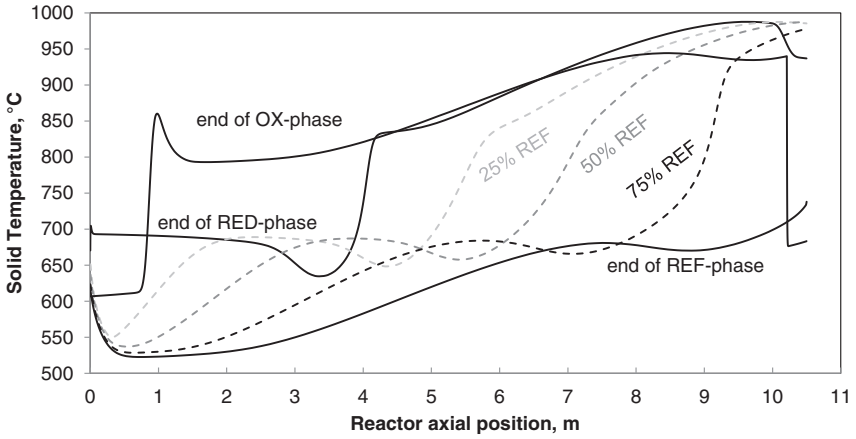

Fig. 13. Axial solid temperature profiles at the end of the reduction (RED), oxidation (OX) and during the reforming phases (respectively at 25%, 50%, 75% and 100% of the cycle time) for the process designed for H_2 production (for conditions see Table 6).

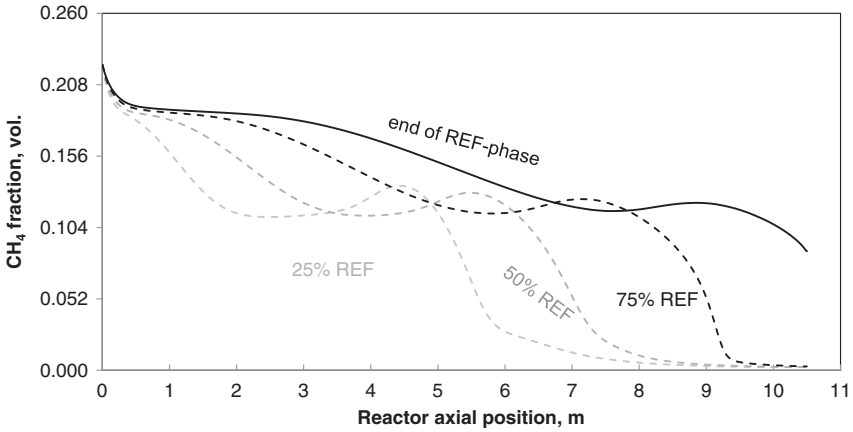

Fig. 14. Axial CH_4 mole fraction profile during the reforming phase at respectively at 25%, 50%, 75% and 100% of the cycle time) for the process designed for H_2 production (operating conditions listed in Table 6).

The gas composition and temperature at the reactor outlet during the consecutive reduction, reforming and oxidation phases are shown in Fig. 15. As in the hydrogen production case, only CO_2 and H_2O are produced during the reduction phase. In this case, the inlet gas consists mostly of H_2O resulting from the methanol synthesis process. The temperature of the gas leaving the reactor is not constant. In particular, it is possible to distinguish two temperature levels at which the gases are released: about 730 °C for the first 130 s and 970 °C for the remaining 145 s of the reduction phase. During the reforming phase, only CO, H_2 and CO_2 (and excess H_2O) are produced, with a M-factor (Eq. (5)) equal to 2.06. After 75% of the time of the reforming phase, CH_4 breakthrough occurs and the M-factor decreases to 1.7 at the end of the reforming phase.

The lower M-factor would decrease the CH_3OH yield. However, as already discussed by the authors in a previous work on CLC for a large-scale power plant [49], relatively stable properties of the gas from PB chemical looping reactors system can be obtained by operating the reactors in the same phase in parallel but with a phase displacement. In this case, by adopting a phase displacement of 55 s it is possible to smooth out the fluctuations, thus reaching the final gas conditions shown in Fig. 16. This strategy is beneficial for the processes downstream of the CLR, which can then be designed for steady state operations. After mixing, an average M-factor of 2 is achieved with the selected operating conditions. The oxidation cycle releases a constant flow rate of N_2-rich stream at about 750 °C, which is expanded in the gas turbine to supply part of the power required in the plant.

As already discussed for the case of H_2 production, the maximum bed temperature is reached at the end of the oxidation phase and the reactor cooling occurs during the reforming phase (Fig. 17). The CH_4 breakthrough during reforming can be explained by inspecting the temperature profile in the last part of the reactor, which reduces from 930 °C at the end of the reduction phase to 820 °C after 75% of the reforming cycle time, which corresponds to the beginning of CH_4 breakthrough, and finally to 730 °C at the end of the reforming phase, where the CH_4 content reaches 11% (vol. basis).

Since large-scale CH_3OH plants are based on a combination of SMR and ATR processes in order to reach the optimal composition for methanol synthesis, retrofitting of existing plants is less demanding than for the case of H_2 production. It mostly relates to the thermal integration due to the presence of the gas turbine cooling units, which are mostly carried out using pressurized gas.

7. Conclusions

In this paper, a novel application of chemical looping reforming for H_2 and CH_3OH production using dynamically operated PBRs has been presented. Multiple experiments for the redox and reforming phases have been carried out. A phenomenological model accounting for radial

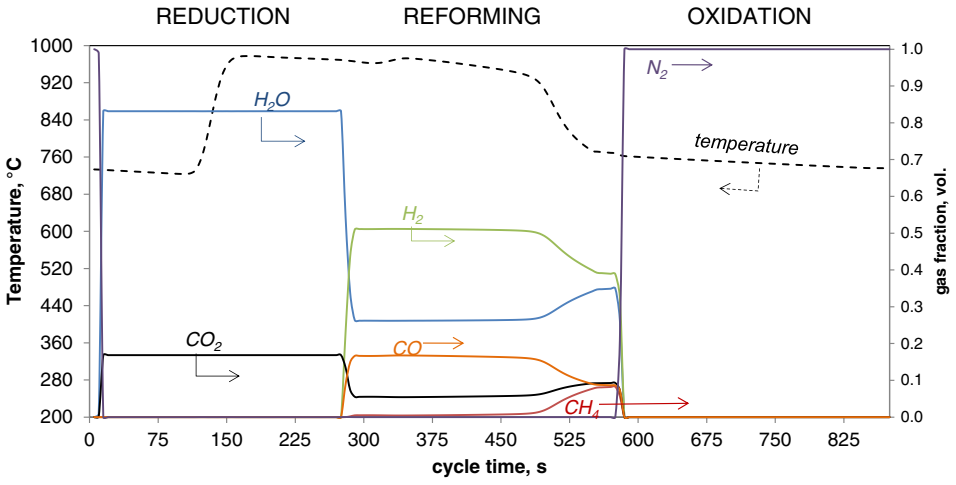

Fig. 15. Gas conditions (temperature and composition) at the reactor outlet for the process designed for CH_3OH production (operating conditions listed in Table 6).

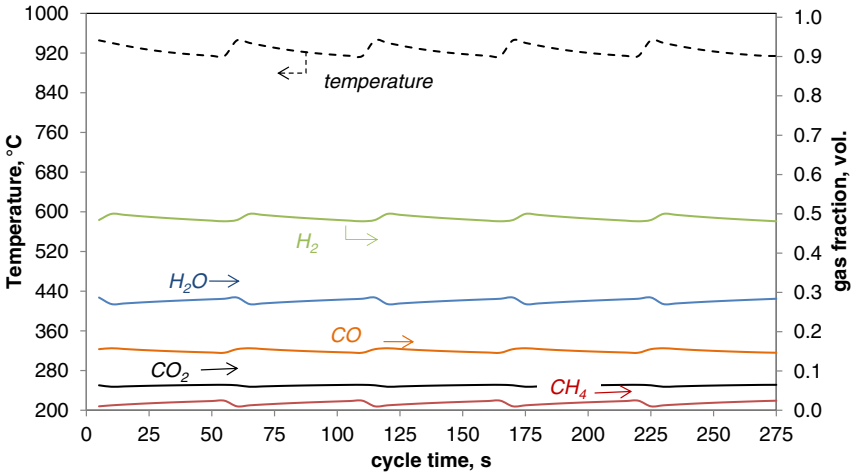

Fig. 16. Gas conditions (temperature and composition) at the CLR plant outlet after mixing 5 streams coming from parallel reactors operated in the reforming phase with a phase displacement of 55 s (conditions of the different phases listed in Table 6).

heat losses has been validated with experiments in which multiple reduction/oxidation/reforming cycles have been carried out at different temperatures and inlet gas compositions. With respect to previous works on chemical looping with packed bed reactors, the present model also includes a dedicated model for the radial heat losses of the reactor reproducing the experimental results obtained in the lab-scale facility. The results from this paper demonstrated that the combination of chemical looping combustion and steam reforming can be accomplished through sequential heat storage and heat removal. In addition to the process description and a first experimental proof-of-principle, a preliminary reactor design for H_2 and CH_3OH production has been proposed and their heat management assessed. The overall performance in terms of CH_4 conversion, CO_2 emissions and H_2/CH_3OH yields has been calculated. For the case of H_2 production, the system reaches a CH_4 conversion during the reforming above 92% and PSA off-gas can be used efficiently as fuel for the reduction phase. For the CH_3OH plant, an overall CH_3OH yield of 89% is reached. In both cases, the flue gases emitted to the environment do not contain CO_2. The produced CO_2 during the reduction phase is separated from H_2O and compressed for further utilization (in case of a smaller-size plant) or final storage. The very good performance of the PB-CLR process associated to the high yields of H_2 or CH_3OH with near-zero CO_2 emissions asks for further assessment of this technology from an economic point of view by means of a complete process integration study and economic analysis.

Nomenclature

AGR acid gas removal
ASU air separation unit
ATR auto-thermal reforming
CCS CO_2 capture and storage
CLC chemical looping combustion
CLR chemical looping reforming
FTR fired tubular reforming
LP/IP/HP low/intermediate/high pressure
LT/IT/HT low/intermediate/high temperature
MEA mono-ethanol-amine
MDEA methyl di-ethanol-amine
MTPD metric tons per day
PBR packed bed reactor
PSA pressure swing adsorption
SMR steam methane reforming
WGS water gas shift

Units

A [m^2] area
b [$mol_s mol_g^{-1}$] gas-solid stoichiometric factor
Bi [−] Biot number

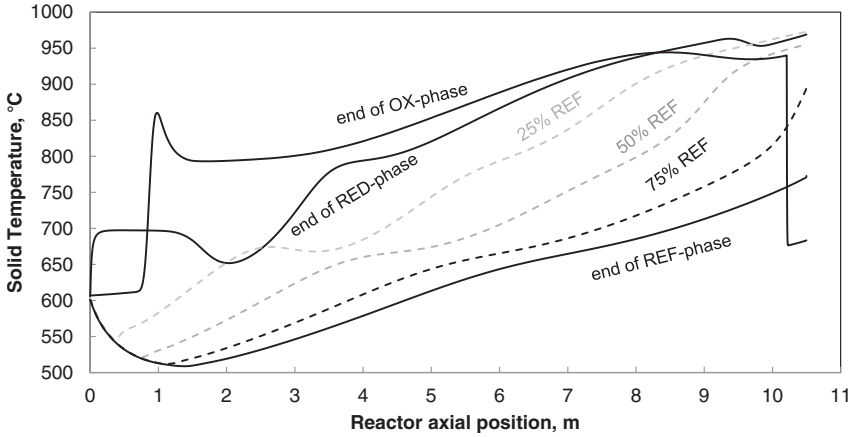

Fig. 17. Axial solid temperature profile at the end of the reduction (RED), oxidation (OX) and during the reforming phases at respectively at 25%, 50%, 75% and 100% of the cycle time for the process designed for CH_3OH production (conditions listed in Table 6).

C [mol m^{-3}] concentration
Cp [J mol^{-1} K^{-1}] heat capacity
d [m] diameter
D [m^2 s^{-1}] diffusion coefficient
D_0 [mol^{1-n} m^{3n-1} s^{-1}] pre-exponential factor for the diffusion term
D_{ax} [m^2 s^{-1}] axial dispersion coefficient
d_p [m] particle diameter
E_A [kJ mol^{-1}] activation energy
E_{Ds} [kJ mol^{-1}] activation energy for the diffusion term
h [W m^{-2} K^{-1}] convective heat transfer coefficient
H [−] reactor height
k_0 [mol^{1-n} m^{3n-1} s^{-1}] pre-exponential factor
k_{rs} [W m^{-1} K^{-1}] radial conductivity of the solid (stagnant conditions)
k_x [−] solid diffusion decay constant
MW [kg mol^{-1}] molecular weight
n [−] reaction order
n_i [mol m^{-2} s^{-1}] gas flux of ith-component
Nu [−] Nusselt number $Nu = \frac{h_g d_p}{\lambda_g}$
P [bar] pressure
Pe [−] Peclet number
Pr [−] Prantl number $\mathrm{Pr} = \frac{C_{p,g}\mu_g}{\lambda_g}$
r_i [mo m^{-3} s^{-1}] reaction rate
R [J mol^{-1} K^{-1}] gas constant
Re [−] Reynolds number $\mathrm{Re} = \frac{\rho_g v_g d_p}{\mu_g}$
R_i [KW^{-1}] thermal resistance
r_i [mol mr^{-3} s^{-1}] reaction rate
r_0 [m] particle radius
Sc [−] Schmidt number $Sc = \frac{\rho_g \mu_g}{D}$
t [s] time
T K or °C temperature
X [−] solid conversion
y_i [−] mol fraction

Greek letters

α [W m^{-2} K^{-1}] global heat transfer coefficient
ε_g [−] void fraction
$\varepsilon_{s,p}$ [−] solid porosity
ε_{steel} [−] emissivity coefficient of the reactor
ε_{oven} [−] emissivity coefficient of the oven
η [kg m^{-1} s^{-1}] dynamic gas viscosity
ζ [mol_g mol_s^{-1}] stoichiometric factor
λ [W m^{-1} K^{-1}] heat dispersion
ρ [kg m^{-3}] density
τ [−] tortuosity

Acknowledgments

The authors are grateful to Johnson Matthey (UK) for supplying the Ni-based catalyst used for the experiments and operation of the system.

Appendix A. Supplementary data

Supplementary data to this article can be found online at doi:10.1016/j.fuproc.2016.10.014.

References

[1] K. Aasberg-Petersen, J.H. Bak Hansen, T.S. Christensen, I. Dybkjaer, P.S. Christensen, C. Stub Nielsen, et al., Technologies for large-scale gas conversion, Appl. Catal. A Gen. 221 (2001) 379–387.
[2] E. Fiedler, G. Grossmann, D. Kersebohm, G. Weiss, C. Witte, Methanol, in: W.-V.V.G., C. KgaA (Eds.),Ullmann's Encyclopedia of Industrial Chemistry, 2000.
[3] Foster Wheeler, Steam-hydrocarbon Reformer Furnace Design, (n.d.) 1–26.
[4] J.R. Rostrup-Nielsen, Production of synthesis gas, Catal. Today 18 (1993) 305–324.
[5] J. Rostrup-Nielsen, New aspects of syngas production and use, Catal. Today 63 (2000) 159–164.
[6] I. Martínez, M.C. Romano, P. Chiesa, G. Grasa, R. Murillo, Hydrogen production through sorption enhanced steam reforming of natural gas: thermodynamic plant assessment, Int. J. Hydrog. Energy 38 (2013) 15180–15199.
[7] A. Carrara, A. Perdichizzi, G. Barigozzi, Simulation of an hydrogen production steam reforming industrial plant for energetic performance prediction, Int. J. Hydrog. Energy 35 (2010) 3499–3508.
[8] DOE/NETL, Assessment of Hydrogen Production With CO_2 Capture Volume 1, Baseline State-of- the-Art Plants, 2010.
[9] K. Aasberg-Petersen, C.S. Nielsen, I. Dybkjær, J. Perregaard, Large Scale Methanol Production from Natural Gas, 2013 1–14.
[10] J.F. Goellner, N.J. Kuehn, V. Shah, C.W. White_III, M.C. Woods, Baseline Analysis of Crude Methanol Production From Coal and Natural Gas, 2014.
[11] J.C. Abanades, B. Arias, A. Lyngfelt, T. Mattisson, D.E. Wiley, H. Li, et al., Emerging CO_2 capture systems, Int. J. Greenh. Gas Control 40 (2015) 126–166.
[12] J. Adanez, A. Abad, F. Garcia-Labiano, P. Gayan, L. de Diego, Progress in chemical-looping combustion and reforming technologies, Prog. Energy Combust. Sci. 38 (2012) 215–282.
[13] M. Ortiz, A. Abad, L.F. de Diego, F. García-Labiano, P. Gayán, J. Adánez, Optimization of hydrogen production by chemical-looping auto-thermal reforming working with Ni-based oxygen-carriers, Int. J. Hydrog. Energy 36 (2011) 9663–9672.
[14] M. Tang, L. Xu, M. Fan, Progress in oxygen carrier development of methane-based chemical-looping reforming: a review, Appl. Energy 151 (2015) 143–156.
[15] T. Pröll, J. Bolhàr-Nordenkampf, P. Kolbitsch, H. Hofbauer, Syngas and a separate nitrogen/argon stream via chemical looping reforming–a 140 kW pilot plant study, Fuel 89 (2010) 1249–1256.
[16] F.-X. Chiron, G.S. Patience, S. Rifflart, Hydrogen production through chemical looping using $NiO/NiAl_2O_4$ as oxygen carrier, Chem. Eng. Sci. 66 (2011) 6324–6330.
[17] L.F. de Diego, M. Ortiz, J. Adánez, F. García-Labiano, A. Abad, P. Gayán, Synthesis gas generation by chemical-looping reforming in a batch fluidized bed reactor using Ni-based oxygen carriers, Chem. Eng. J. 144 (2008) 289–298.
[18] M. Ortiz, L.F. de Diego, A. Abad, F. García-Labiano, P. Gayán, J. Adánez, Hydrogen production by auto-thermal chemical-looping reforming in a pressurized fluidized bed reactor using Ni-based oxygen carriers, Int. J. Hydrog. Energy 35 (2010) 151–160.
[19] A. Hafizi, M.R. Rahimpour, S. Hassanajili, Hydrogen production via chemical looping steam methane reforming process: effect of cerium and calcium promoters on the performance of Fe_2O_3/Al_2O_3 oxygen carrier, Appl. Energy 165 (2016) 685–694.
[20] Z. Zhou, L. Han, G.M. Bollas, Kinetics of NiO reduction by H_2 and Ni oxidation at conditions relevant to chemical-looping combustion and reforming, Int. J. Hydrog. Energy 39 (2014) 8535–8556.
[21] M. Rydén, A. Lyngfelt, T. Mattisson, D. Chen, A. Holmen, E. Bjørgum, Novel oxygen-carrier materials for chemical-looping combustion and chemical-looping reforming; $LaxSr_{1-x}FeyCo_{1-y}O_{3-\delta}$ perovskites and mixed-metal oxides of NiO, Fe_2O_3 and Mn_3O_4, Int. J. Greenh. Gas Control 2 (2008) 21–36.
[22] J.A. Medrano, V. Spallina, M. van Sint Annaland, F. Gallucci, Thermodynamic analysis of a membrane-assisted chemical looping reforming reactor concept for combined H_2 production and CO_2 capture, Int. J. Hydrog. Energy 39 (2014) 4725–4738.
[23] M. Ryden, A. Lyngfelt, Using steam reforming to produce hydrogen with carbon dioxide capture by chemical-looping combustion, Int. J. Hydrog. Energy 31 (2006) 1271–1283.
[24] M. Ryden, A. Lyngfelt, T. Mattisson, Synthesis gas generation by chemical-looping reforming in a continuously operating laboratory reactor, Fuel 85 (2006) 1631–1641.
[25] R.F. Kooiman, H.P. Hamers, F. Gallucci, M. van Sint Annaland, Experimental demonstration of two-stage packed bed chemical-looping combustion using syngas with CuO/Al_2O_3 and $NiO/CaAl_2O_4$ as oxygen carriers, Ind. Eng. Chem. Res. 54 (2015) 2001–2011.
[26] F. Gallucci, H.P. Hamers, M. van Zanten, M. van Sint Annaland, Experimental demonstration of chemical-looping combustion of syngas in packed bed reactors with ilmenite, Chem. Eng. J. 274 (2015) 156–168.
[27] V. Spallina, M.C. Romano, P. Chiesa, F. Gallucci, M. Van Sint Annaland, G. Lozza, Integration of coal gasification and packed bed CLC for high efficiency and near-zero emission power generation, Int. J. Greenh. Gas Control 27 (2014) 28–41.
[28] H.P. Hamers, F. Gallucci, P.D. Cobden, E. Kimball, M. van Sint Annaland, A novel reactor configuration for packed bed chemical-looping combustion of syngas, Int. J. Greenh. Gas Control 16 (2013) 1–12.
[29] G. Diglio, P. Bareschino, E. Mancusi, F. Pepe, Simulation of hydrogen production through chemical looping reforming process in a packed-bed reactor, Chem. Eng. Res. Des. 105 (2015) 137–151.
[30] H.P. Hamers, F. Gallucci, P.D. Cobden, E. Kimball, M. van Sint Annaland, CLC in packed beds using syngas and CuO/Al_2O_3: model description and experimental validation, Appl. Energy 119 (2014) 163–172.
[31] S. Noorman, M. Van Sint Annaland, J.A.M. Kuipers, Experimental validation of packed bed chemical-looping combustion, Chem. Eng. Sci. 65 (2010) 92–97.
[32] J. Smit, M. van Sint Annaland, J.A.M. Kuipers, Grid adaptation with WENO schemes for non-uniform grids to solve convection-dominated partial differential equations, Chem. Eng. Sci. 60 (2005) 2609–2619.
[33] D. Vortmeyer, R. Berninger, Comments on the paper, theoretical prediction of effective heat transfer parameters in packed beds by Anthony Dixon and D. L. Cresswell, AICHE J. 28 (1982) 508–510.
[34] D.J. Gunn, M.A. Misbah, Bayesian estimation of heat transport parameters in fixed beds, Int. J. Heat Mass Transf. 36 (1993) 2209–2221.
[35] D.J. Gunn, Transfer of heat or mass to particles in fixed and fluidised beds, Int. J. Heat Mass Transf. 21 (1978) 467–476.

[36] M.F. Edwards, J.F. Richardson, Gas dispersion in packed beds, Chem. Eng. J. 23 (1968) 109–123.
[37] J.A. Medrano, H.P. Hamers, G. Williams, M. van Sint Annaland, F. Gallucci, NiO/$CaAl_2O_4$ as active oxygen carrier for low temperature chemical looping applications, Appl. Energy 158 (2015) 86–96.
[38] T. Numaguchi, K. Kikuchi, Intrinsic kinetics and design simulation in a complex reaction network: steam-methane reforming, Chem. Eng. Sci. 43 (1988) 2295–2301.
[39] A. Donazzi, A. Beretta, G. Groppi, P. Forzatti, Catalytic partial oxidation of methane over a 4% Rh/??-Al_2O_3 catalyst part II: role of CO_2 reforming, J. Catal. 255 (2008) 259–268.
[40] A.G. Dixon, D.L. Cresswell, Theoretical prediction of effective heat transfer parameters in packed beds, AlCHE J. 25 (1979) 663–676.
[41] A.G. Dixon, Thermal resistance models of packed bed effective heat transfer parameters.pdf, AlCHE J. 31 (1985) 826–834.
[42] S. Yagi, N. Wakao, Heat and mass transfer from wall to fluid in packed beds, AlCHE J. 5 (1959) 79–85.
[43] P. Zehner, E.U. Schlünder, Wärmeleitfähigkeit von Schüttungen bei mäßigen Temperaturen, Chemie Ing. Tech. 42 (1970) 933–941.
[44] S. Noorman, F. Gallucci, M. van Sint Annaland, J.A.M. Kuipers, Experimental investigation of chemical-looping combustion in packed beds: a parametric study, Ind. Eng. Chem. Res. 50 (2011) 1968–1980.
[45] J.R. Fernández, J.C. Abanades, R. Murillo, G. Grasa, Conceptual design of a hydrogen production process from natural gas with CO_2 capture using a Ca–Cu chemical loop, Int. J. Greenh. Gas Control 6 (2012) 126–141.
[46] H.P. Hamers, F. Gallucci, G. Williams, P.D. Cobden, M. van Sint Annaland, Reactivity of oxygen carriers for chemical-looping combustion in packed bed reactors under pressurized conditions, Energy Fuel 29 (2015) 2656–2663.
[47] M.A. Pans, A. Abad, L.F. de Diego, F. García-Labiano, P. Gayán, J. Adánez, Optimization of H_2 production with CO_2 capture by steam reforming of methane integrated with a chemical-looping combustion system, Int. J. Hydrog. Energy 38 (2013) 11878–11892.
[48] V. Spallina, F. Gallucci, M.C. Romano, P. Chiesa, G. Lozza, M. van Sint Annaland, Investigation of heat management for CLC of syngas in packed bed reactors, Chem. Eng. J. 225 (2013) 174–191.
[49] V. Spallina, P. Chiesa, E. Martelli, F. Gallucci, M.C. Romano, G. Lozza, et al., Reactor design and operation strategies for a large-scale packed-bed CLC power plant with coal syngas, Int. J. Greenh. Gas Control 36 (2015) 34–50.